Hindawi
International Transactions on Electrical Energy Systems
Volume 2022, Article ID 8131611, 14 pages
https://doi.org/10.1155/2022/8131611

Research Article

Analysis and Verification of Compound SRFPI-LADRC Strategy for an Off-Grid Single-Phase Inverter

Liaoyuan Lin, Haoda Li, Kai Zhu, Lingling Shi, and Ping Li

College of Information Science and Engineering, Huaqiao University, Xiamen, China

Correspondence should be addressed to Liaoyuan Lin; lly3806@foxmail.com

Received 30 March 2022; Revised 24 August 2022; Accepted 10 September 2022; Published 13 October 2022

Academic Editor: Subrata Kumar Sarker

Summary. The linear active disturbance rejection control (LADRC) is mainly applied for tracking a step signal, and it is inadequate to realize satisfactory performance in the control of a single-phase inverter whose reference signal is sinusoidal. In this paper, an improved voltage control strategy based on compound synchronous reference frame proportional-integral (SRFPI) control and LADRC is proposed. The SRFPI and LADRC remain relatively independent without complicating the control parameter design. Detailed theoretical analyses on the compound strategy and its performance are presented, indicating that it inherits the advantages of the two controllers. Moreover, contrast experiments are carried out to verify the feasibility and superiority of the proposed control strategy. The results show that the system achieves a small steady-state error, voltage tracking error, fast transient response, and low total harmonic distortion (THD) when feeding a highly nonlinear load.

1. Introduction

Single-phase inverters, as core components, are extensively employed in various applications including industrial facilities such as uninterrupted power supply (UPS) [1,2] and renewable energy fields in terms of distributed generations (DGs) and microgrids (MGs) [3, 4]. To summarize, it is mainly adopted to supply a stable and high-quality sinusoidal voltage for ac loads. [5, 6] Therefore, a proper control technique for regulating the output voltage of single-phase inverters is quite important.

Recently, a variety of control methods have been investigated for better performance of inverters. Thanks to implementation simplicity and high reliability, conventional single or dual closed-loop control systems are going with the proportional-integral-derivative (PID) regulators [7, 8]. However, it is difficult to maintain the optimality of system performance in terms of steady errors and total harmonic distortion (THD), especially under nonlinear load conditions. Surrounding the above problems, the deadbeat control (DBC), the proportional-resonant (PR) control, and the repetitive control (RC) are the main solutions. Owing to direct regulation of the instantaneous output voltage and optimal tuning, the DBC provides superior dynamic performance [9, 10]. Despite that, it is more prone to produce a steady-state error and suffers from the sensitivity of parameter variation. The PR control possesses excellent steady-state performance by introducing an infinite gain at the fundamental frequency. [11, 12] Note that multiple resonant units are required for harmonic suppression, which inevitably leads to complexity or even instability, and PR control is also constrained by sensitivity to deviations of sensed signals [13]. On the basis of the internal model principle, the RC can get rid of distortions and steady-state errors in the periodic output voltage [14, 15]. However, it exhibits inadequate performance such as slow transient response and poor tracking accuracy in the presence of aperiodic disturbances, which intensely affects its applications. In addition, some optimal controllers such as the model predictive control (MPC), the linear quadratic Gaussian (LQG) controller, and the optimal PID controllers are presented in the literature. The MPC has been extensively implemented in the

control of inverters due to its simplicity and robustness [16]. Nevertheless, the computation and time cost need to be further improved for the real-time and online control platform. The LQG combines the advantages of the Kalman state estimation and the optimal linear quadratic regulator. Thus, it exhibits improved robustness and provides a fast transient response [17]. Moreover, intelligence algorithms have been introduced to realize optimal parameters for the self-turning of PID controllers for inverters [18]. However, these methods show higher complexity and cannot remove the steady-state tracking error.

Currently, the synchronous reference frame proportional-integral (SRFPI) control has been broadly adapted and maturely developed in three-phase inverters. This method also increasingly appears in single-phase inverter applications [13, 19, 20]. The steady-state error can be removed by employing PI regulators in the synchronous reference frame (SRF) [21]. However, generating a virtual orthogonal signal, particularly the orthogonal current signal, may result in slow dynamic performance. Meanwhile, it has limited rejection ability with disturbances. Table 1 shows the comparison of the typical control schemes for single-phase inverters.

Han comprehensively and systematically introduced the active disturbance rejection control (ADRC) method in 1999 [22]. It does not require the exact system mathematical model. After that, Gao proposed linear ADRC (LADRC) based on the linearization of the extended state observer (ESO) and the controller, which greatly simplified the parameter setting [23, 24]. It treats internal and external disturbances as the total disturbance and utilizes the input and output targets to estimate the disturbances for disturbance rejection [25]. In addition, as a general-purposed control structure [26], the LADRC has been widely used in control systems with step reference signals such as servo systems [27, 28] and three-phase inverters in the SRF [29, 30] but relatively few in single-phase inverters [31–33]. The main reason is that it is unable to eliminate the steady-state error when tracking a sinusoidal signal. In Ref. 31, a step-by-step analysis of the classic LADRC for a single-phase inverter is presented. However, there exists a non-negligible steady-state error in the output voltage. An improved control law using reference differential feedforward for a grid-tied inverter is proposed in Ref. 32 to reduce the steady-state error. Its performance used in off-grid inverters needs further verification. In Ref. 33, a repetitive learning controller is embedded in LADRC to achieve a high-quality output voltage and robustness. However, this approach adds complexity to the LADRC design.

To improve the performance of LADRC used in an off-grid single-phase inverter, in this paper, an improved voltage control strategy based on compound SRFPI and LADRC is proposed. The performance verification of this method is focused on the inverter under resistive load, nonlinear load, and step load (no load to resistive load). The salient features of the proposed method are as follows:

(1) The output of SRFPI serves as the voltage reference of LADRC. In terms of control structure, SRFPI and LADRC are relatively independent, which does not complicate the controller design of LADRC.

(2) The proposed method does not contain current loops. Therefore, it does not need to generate the current quadrature signals that may affect the dynamic response. Moreover, high precision and high-cost current sensors are not required for waveform control under normal conditions. It is still necessary to measure the inductor current for overcurrent protection, but more economical ways can be adopted. This part is out of the scope of this paper.

(3) The compound method fuses the merits of both two controllers. Theoretical analysis, simulation, and experimental results are provided to confirm that the proposed scheme brings an overall performance improvement in terms of tracking error, steady-state error, dynamic response as well as voltage THD, especially when feeding highly nonlinear loads.

This paper is organized as follows: the implementation of LADRC in a single-phase inverter is introduced in Section 2. The proposed compound control strategy and corresponding theoretical analysis are given in Section 3. Experimental results are discussed in Section 4. Finally, conclusions are summarized in Section 5.

2. Implementation of LADRC in Single-Phase Inverters

2.1. Modelling of Single-Phase Inverters. A single-phase inverter that consists of the insulated-gate bipolar transistor (IGBT) full-bridge frame with an *LC* output filter is shown in Figure 1. V_{dc}, v_{in}, v_o, i_L, and $i_o$denote the dc link voltage, input voltage, output voltage, inductor current, and output current; r_e, L, and C denote the equivalent series resistance, filter inductor, and filter capacitor, respectively. According to Kirchhoff's laws, the differential equations describing the dynamics of a single-phase inverter can be written as

$$\begin{cases} L\dfrac{\mathrm{d}i_L}{\mathrm{d}t} = v_{in} - v_o - r_e i_L \\ \\ C\dfrac{\mathrm{d}v_o}{\mathrm{d}t} = i_L - i_o \end{cases} \tag{1}$$

The relation between the sinusoidal modulation signal v_m and v_{in} can be derived as a PWM proportional gain: $K_{PWM} = v_{in}/v_m = V_{dc}/V_t$, where V_t is the amplitude of the triangular carrier, and its value is set to 1. To obtain a better voltage regulation, a proportional gain $1/V_{dc}$ is connected in series with the control signal u. Considering i_o as the input disturbance, the equivalent model of the inverter is illustrated in Figure 2. The transfer function of the plant can be obtained as

$$G_p(s) = \frac{v_o(s)}{v_{in}(s)} = \frac{v_o(s)}{u(s)} = \frac{1}{LCs^2 + r_e Cs + 1}. \tag{2}$$

According to (2), the differential form of the transfer function of the inverter can be described as

Table 1: Feature comparison of control schemes for single-phase inverters.

Comparative item	Deadbeat control	PR control	Repetitive control	MPC	SRFPI control
Hardware cost	High	Low	Low	Low	Low
Sensitivity of parameter variation	Strong	Medium	Low	Medium	Medium
Steady-state performance	Medium	Medium	Good	Medium	Good
Transient performance	Good	Medium	Worse	Good	Good
Virtual orthogonal signals	Not required	Not required	Not required	Not required	Required

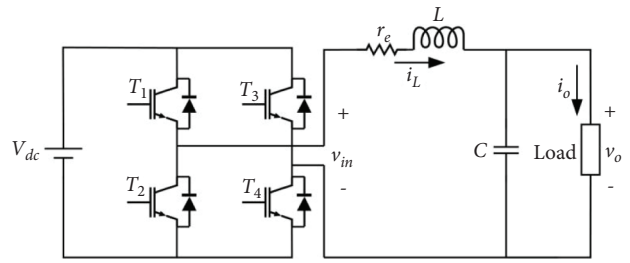

Figure 1: Single-phase inverter with the *LC* filter.

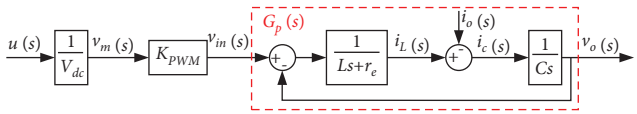

Figure 2: Equivalent block diagram of the single-phase inverter.

$$\ddot{v}_o = -a_1\dot{v}_o - a_0 v_o + b_0 u, \tag{3}$$

where $a_0 = b_0 = 1/LC$ and $a_1 = r_e/L$.

2.2. Design of LESO. The core idea of LADRC is to implement a linear extended state observer (LESO) for estimating state variables and total disturbance of the system, and then a forward feedback rejection is built for disturbance compensation.

As seen in (2) and (3), the control object is a second-order system, and it is a nonstandard integral series system ($\ddot{v}_o = b_0 u$). In general, LESO takes full advantage of the system model to calculate control variables and treats the parts different from the standard integral series system as disturbances. Thus, the known disturbances can be expressed as $f_0(\dot{v}_o, v_o) = -a_1\dot{v}_o - a_0 v_o$, where a_0 and a_1 are the known parameters. There are many unknown internal and external disturbances such as parameter perturbation, sampling noise, and unmodeled dynamics during the actual operation of the inverter. The unclear disturbances are denoted by d. The value of b_0 can be directly obtained from the actual inverter system while the unclear part of the system model is described as b_1. To sum up, the actual total unknown disturbance can be defined as $f_1 = d + b_1 u$. Regarding $f = f_1 + f_0(\dot{v}_o, v_o)$ as the total disturbance of the system, the actual inverter system can be rewritten as

$$\ddot{v}_o = b_0 u + f. \tag{4}$$

Let $x = [x_1 x_2 x_3]^{\mathrm{T}} = [v_o \dot{v}_o f\ ]^{\mathrm{T}}$ and $y = v_o$. The disturbance can be added to the following state space representation by introducing an extended state as

$$\begin{cases} \dot{x} = A_p x + B_p u + E_p \dot{f}_1, \\ y = C_p x, \end{cases} \tag{5}$$

where

$$A_p = \begin{bmatrix} 0 & 1 & 0 \\ 0 & 0 & 1 \\ 0 & -a_0 & -a_1 \end{bmatrix}, B_p = \begin{bmatrix} 0 \\ b_0 \\ -a_1 b_0 \end{bmatrix}, E_p = \begin{bmatrix} 0 \\ 0 \\ 1 \end{bmatrix}, C_p = [\,1 \ 0 \ 0\,]. \tag{6}$$

From (5), system matrix A_p contains the known model coefficients (a_0, a_1). Let $\hat{x} = [\,\hat{x}_1 \ \hat{x}_2 \ \hat{x}_3\,]^T = [\,\hat{v}_o \ \hat{\dot{v}}_o \ \hat{f}\,]^T$ and $L_p = [\,l_{p1} \ l_{p2} \ l_{p3}\,]^T$. The model-assisted LESO (MA-LESO) is designed as

$$\begin{cases} \dot{\hat{x}} = A_p\hat{x} + B_p u + L_p(y - \hat{y}) = (A_p - L_p C_p)\hat{x} + B_p u + L_p y, \\ \hat{y} = C_p\hat{x}, \end{cases} \tag{7}$$

where $\hat{x}$ and L_p denote the observed state variable and gain matrix of the LESO. The eigenvalues of A_p-L_pC_p determine the decay rate of the observed error. To simplify the analysis, its poles are arranged at the same position as

$$\lambda(s) = |sI - A_p + L_p C_p| = (s + \omega_o)^3, \tag{8}$$

where ω_o is the bandwidth of the observer. It can be derived that

$$\begin{cases} l_1 = 3\omega_o - a_1, \\ l_2 = 3\omega_o^2 - 3a_1\omega_o - a_0 + a_1^2, \\ l_3 = \omega_o^3 - 3a_1\omega_o^2 + 3(a_1^2 - a_0)\omega_o + 2a_0 a_1 - a_1^3. \end{cases} \tag{9}$$

By selecting an appropriate ω_o, the LESO can realize rapid real-time estimations of system state variables and the total disturbance.

2.3. Design of the Control Signal. Based on the observed state variables and disturbance, the control signal u and error feedback control law u_c are designed as shown in Equation (10). Substituting u into Equation (4), the system turns into standard integral series type ($\ddot{v}_o = b_0 u + f \approx u_c$).

$$u = \frac{-\hat{x}_3 + u_c}{b_0} = \frac{-\hat{x}_3 + k_1(r - \hat{x}_1) - k_2\hat{x}_2}{b_0}, \tag{10}$$

where r is the reference signal, and k_1 and k_2 denote the error feedback gain coefficient. The bandwidth tuning method in Ref. 24 is adopted to further simplify the controller

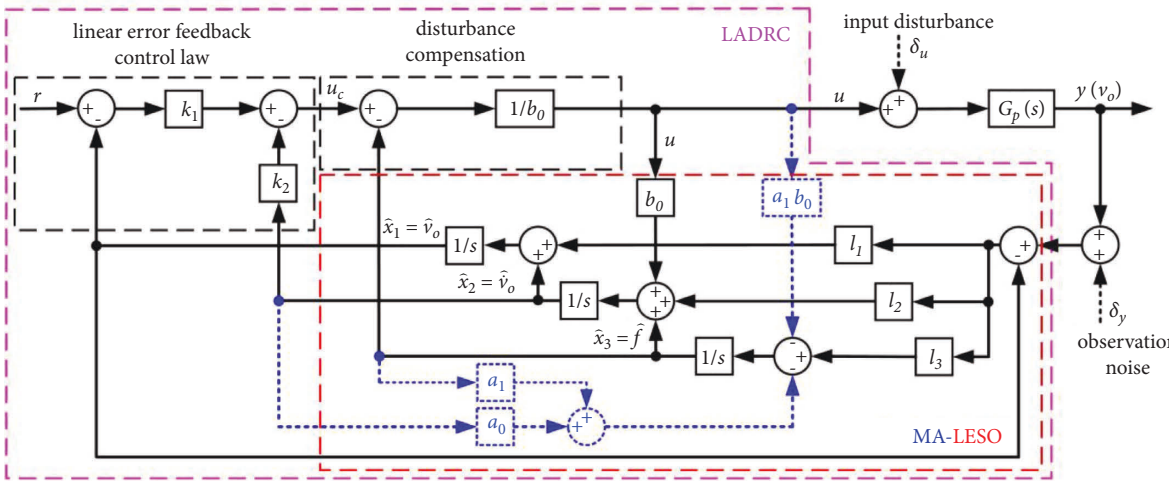

Figure 3: Control block diagram of LADRC for the single-phase inverter.

parameter design, where $k_1 = 2\omega_c{}^2$, $k_2 = 2\omega_c$, and ω_c denotes the controller bandwidth.

In summary, the control block diagram of LADRC for a single-phase inverter mainly contains the error feedback control law, the disturbance compensation block, and MA-LESO, which can be illustrated in Figure 3. For investigating the performance of the LESO, the input disturbance δ_u and the observation noise δ_y are considered, as advised in Ref. 32.

2.4. Performance Analysis of LESO. The deviations between observed values and actual state variables directly affect the control performance of LADRC. The observation error of the output voltage is defined as $x_{e1} = \hat{x}_1 - x_1$. To analyze the effect of the bandwidth ω_o on LESO performance, the observation accuracy of output voltage can be studied with the transfer function of x_{e1}/f_1. Moreover, the disturbance rejection performance can be investigated through the transfer functions of $\hat{x}_1/\delta_u$ and $\hat{x}_1/\delta_y$. According to Equations (5)–(10), the following three transfer functions can be obtained as

$$\begin{cases} \dfrac{x_{e1}}{f_1} = -\dfrac{s}{(s+\omega_o)^3}, \\ \dfrac{\hat{x}_1}{\delta_u} = \dfrac{b_0 s}{(s+\omega_o)^3}, \\ \dfrac{\hat{x}_1}{\delta_y} = \dfrac{(3\omega_o + a_1)s^2 + (a_0 + 3\omega_o{}^2)s + \omega_o{}^3}{(s+\omega_o)^3}. \end{cases} \tag{11}$$

In this study, the inverter parameters are chosen as $L = 0.7$mH, $C = 40\,\mu$F, and $r_e = 0.1\,\Omega$. The Bode diagrams of x_{e1}/f_1, $\hat{x}_1/\delta_u$, and/δ_y with ω_o ranging from 8000 to 14000 rad/s are depicted in Figures 4 and 5, respectively. From Figure 4, it can be seen a larger ω_o makes the observed value $\hat{x}_1$ close to x_1. In other words, f_1 is well estimated and compensated due to the tiny gain in the low-frequency region. However, the estimated ability gets ordinary when the disturbances

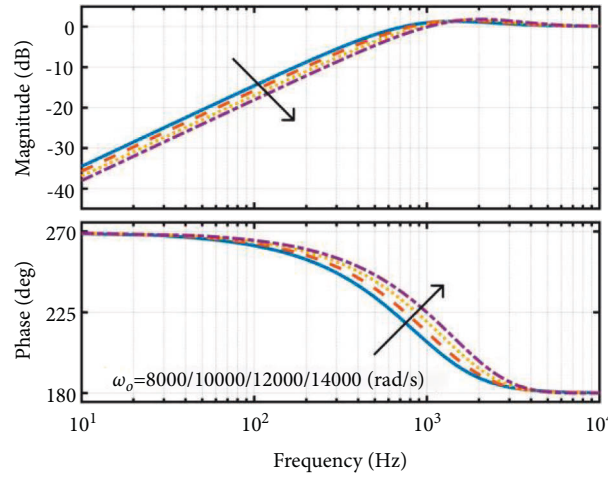

Figure 4: Phase-frequency characteristics of x_{e1}/f_1.

contain high-frequency signals. As shown in Figure 5(a), when a larger ω_o is chosen, the LESO achieves enhanced input disturbance rejection in the low-frequency band, but it has little impact on the high-frequency domain. Clearly, as seen from Figure 5(b), the high-frequency observation noise will be amplified as ω_o increases, while the LESO represents insensitivity to observation noise in the low-frequency region. Therefore, a proper bandwidth of the LESO should compromise the disturbance estimation performance and the measurement noise sensitivity. In this study, $\omega_o = 10000$ rad/s is selected.

2.5. Analysis of the Steady-State Error. The tracking error of the inverter system is defined as $e = r - v_o$. According to (4) and (10), the transfer function of e can be obtained as

$$e(s) = \frac{s^2 + k_2 s}{s^2 + k_2 s + k_1} r(s). \tag{12}$$

Clearly, the LADRC-based voltage control for a single-phase inverter cannot eliminate the steady-state error since the reference signal r is sinusoidal.

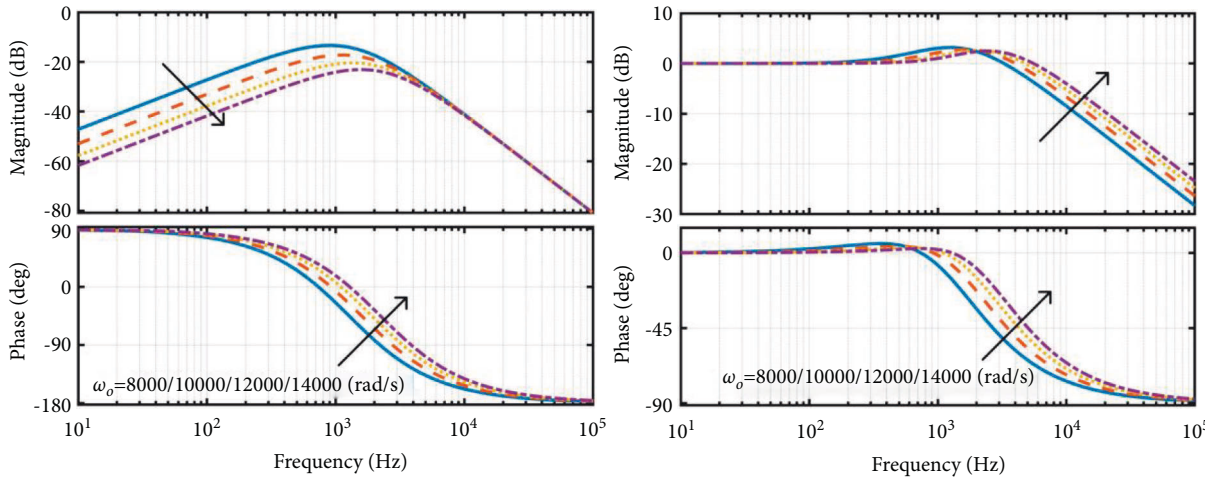

Figure 5: Phase-frequency characteristics of (a) $\widehat{x}_1/\delta_u$ and (b) $\widehat{x}_1/\delta_y$.

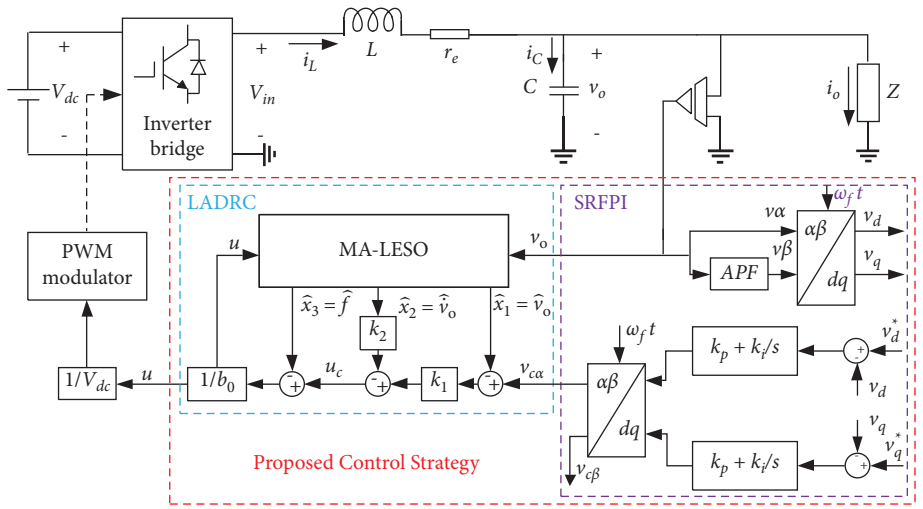

Figure 6: Proposed voltage control structure based on combined SRFPI and LADRC.

3. Design and Analysis of SRFPI-LADRC

As described above, a single-phase inverter with LADRC is contaminated by the steady-state error. In this paper, a compound control strategy is proposed as shown in Figure 6, where the output voltage $v_{c\alpha}$ of SRFPI is employed as the voltage reference of LADRC. In terms of control structure, the SRFPI and the LADRC are relatively independent. The control structure combines the superiority of both controllers, namely disturbance resisting ability and cancellation of the steady-state error.

3.1. Analysis of the SRPFI Controller. Control of single-phase inverters in direct-quadrature SRF is not as well developed as three-phase applications. More complicated structures and the demand for virtual orthogonal signals are the main reasons. The conventional orthogonal-signal-generation (OSG) approach utilizes a delay block to produce an imaginary orthogonal signal. In this study, the all-pass filter (APF)-based OSG is adopted. It is straightforward and attenuates no higher-order components. [34] The structure of the first-order AFP is illustrated in Figure 7, and its transfer function is as follows:

$$H_{APF}(s) = \frac{v_\beta(s)}{v_\alpha(s)} = \frac{\omega_f - s}{\omega_f + s}, \tag{13}$$

where ω_f is the fundamental angular frequency.

To conquer the difficulties of stability analysis of the system when the voltage loop serves in the SRF, the advised method in Ref. 19 is used. The equivalent control block of SRFPI is depicted in Figure 8, where v_r, k_p, and k_i are the set reference, proportional, and integral coefficient of the PI controller, respectively. The SRFPI can be derived in the time domain as

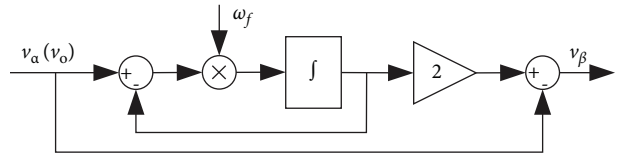

Figure 7: Structure of a first-order APF.

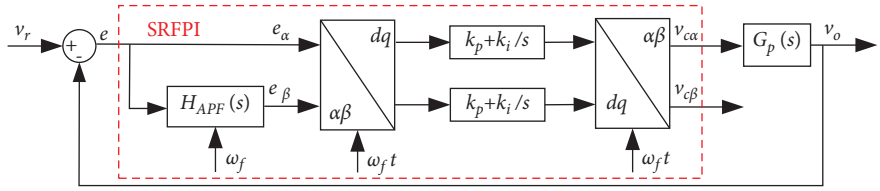

Figure 8: The equivalent control block of SRFPI.

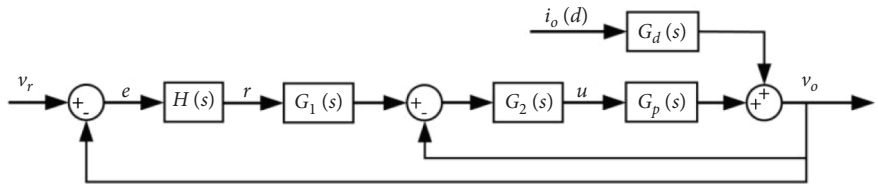

Figure 9: Block diagram of the proposed control system.

$$\begin{bmatrix} v_{c\alpha}(t) \\ v_{c\beta}(t) \end{bmatrix} = \begin{bmatrix} \cos(\omega_f t) & -\sin(\omega_f t) \\ \sin(\omega_f t) & \cos(\omega_f t) \end{bmatrix} \cdot \left\{ \begin{bmatrix} G_{PI}(t) & 0 \\ 0 & G_{PI}(t) \end{bmatrix} * \left\{ \begin{bmatrix} \cos(\omega_f t) & \sin(\omega_f t) \\ -\sin(\omega_f t) & \cos(\omega_f t) \end{bmatrix} \begin{bmatrix} e_\alpha(t) \\ e_\beta(t) \end{bmatrix} \right\} \right\}, \tag{14}$$

where $*$ is the convolution operator.

Taking Laplace transform and substituting $G_{PI}(s) = k_p + k_i/s$, (14) can be described in the s-domain as

$$\begin{bmatrix} v_{c\alpha}(s) \\ v_{c\beta}(s) \end{bmatrix} = \begin{bmatrix} k_p + \dfrac{k_i s}{s^2+\omega_f^2} & -\dfrac{k_i \omega_f}{s^2+\omega_f^2} \\ \dfrac{k_i \omega_f}{s^2+\omega_f^2} & k_p + \dfrac{k_i s}{s^2+\omega_f^2} \end{bmatrix} \begin{bmatrix} e_\alpha(s) \\ e_\beta(s) \end{bmatrix}. \tag{15}$$

By substituting Equation (13) into (15), the transfer function $H(s)$ can be written as

$$H(s) = \frac{v_{c\alpha}(s)}{e_\alpha(s)} = \frac{c_3 s^3 + c_2 s^2 + c_1 s + c_0}{\left(s^2+\omega_f^2\right)\left(s+\omega_f\right)}, \tag{16}$$

where $c_3 = k_p$, $c_2 = k_p\omega_f + k_i$, $c_1 = k_p\omega_f{}^2 + 2\omega_f k_i$, $c_0 = k_p\omega^3{}_f - k_i\omega^2{}_f$. According to (16) and Figure 8, the transfer function $e(s)/v_r(s)$ can be derived. Substituting $s = j\omega_f$ into $e(s)/v_r(s)$ yields

$$\frac{e(s)}{v_r(s)}\Big|_{s=j\omega_f} = \frac{1}{1+H(s)G_pc(s)}\Big|_{s=j\omega_f} = 0. \tag{17}$$

(15) clearly shows that the system realizes zero fundamental voltage tracking error based on the SRFPI control strategy in a steady state.

3.2. Design of SRPFI-LADRC. To obtain the transfer function of the whole system, the following equations can be obtained by substituting Equations (11) into (7).

$$\begin{bmatrix} \dot{\hat{x}}_1 \\ \dot{\hat{x}}_2 \\ \dot{\hat{x}}_3 \end{bmatrix} = \begin{bmatrix} -l_1 & 1 & 0 \\ -l_2 - k_1 & -k_2 & 0 \\ -l_3 + a_1k_1 & -a_0 + a_1k_2 & 0 \end{bmatrix} \begin{bmatrix} \hat{x}_1 \\ \hat{x}_2 \\ \hat{x}_3 \end{bmatrix} + \begin{bmatrix} 0 & l_1 \\ k_1 & l_2 \\ -a_1k_1 & l_3 \end{bmatrix} \begin{bmatrix} r \\ y \end{bmatrix}. \tag{18}$$

Taking the Laplace transform from both sides of Equations (18), $G_1(s)$ and $G_2(s)$ can be derived as

$$\begin{cases} G_1(s) = \dfrac{-v_o(s)}{r(s)} = \dfrac{h_3 s^3 + h_2 s^2 + h_1 s + h_0}{g_2 s^2 + g_1 s + g_0}, \\ G_2(s) = \dfrac{u(s)}{-v_o(s)}, \\ = \dfrac{g_2 s^2 + g_1 s + g_0}{b_0 s^3 + (b_0k_2 + b_0l_1)s^2 + (b_0k_1 + b_0l_2 + b_0k_2l_1)s}, \end{cases} \tag{19}$$

where $h_3 = k_1$, $h_2 = a_1k_1 + k_1l_1$, $h_1 = a_0k_1 + k_1l_2 + a_1k_1l_1$, and $h_0 = k_1l_3 + a_0k_1l_1 + a_1k_1l_2$. $g_2 = l_3 + k_1l_1 + k_2l_2$, $g_1 = k_1l_2 + k_2l_3 - a_0l_2 + a_1k_1l_1 + a_1k_2l_2$, and $g_0 = k_1l_3 + a_0k_1l_1 + a_1k_1l_2$, respectively.

Table 2: Parameters of the inverter system.

Parameters	Values	Parameters	Values
Switching frequency, f_s	20 kHz	DC-link voltage, V_{dc}	190 V
Fundamental angular frequency, ω_f	100π rad/s	The bandwidth of the controller, ω_c	5500 rad/s
Filter inductance, L	700 μH	The bandwidth of the observer, ω_o	10000 rad/s
Filter capacitance, C	40 μF	The proportional factor of the PI controller, k_p	1.5
ESR of the inductance, r_e	0.1 Ω	Integral factor of the PI controller, k_i	100
Voltage reference, v_d^*/v_q^*	156 V/0 V	Dead time, t_d	1.3 μs

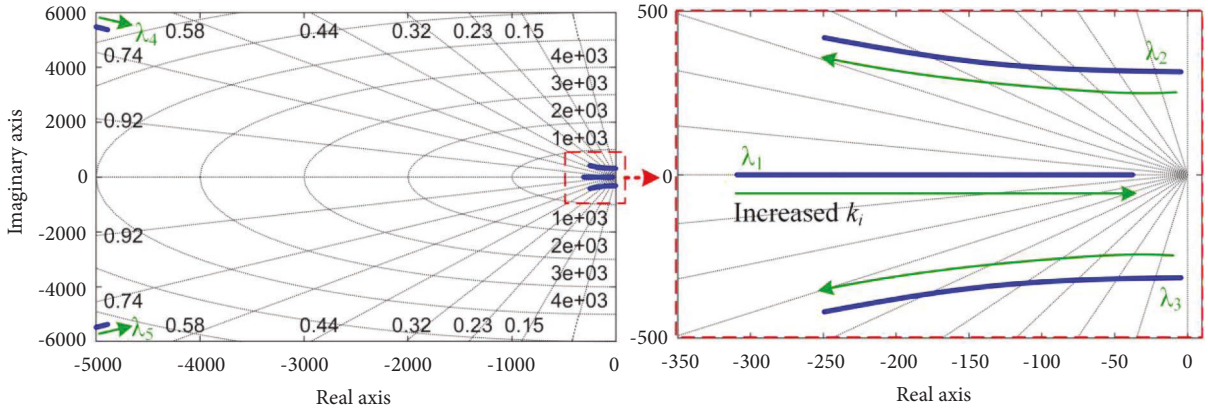

Figure 10: Generalized root locus diagram with a variation of k_i ($10 \le ki \le 500$, $k_p = 1.5$, and $\omega_c = 5500$ rad/s).

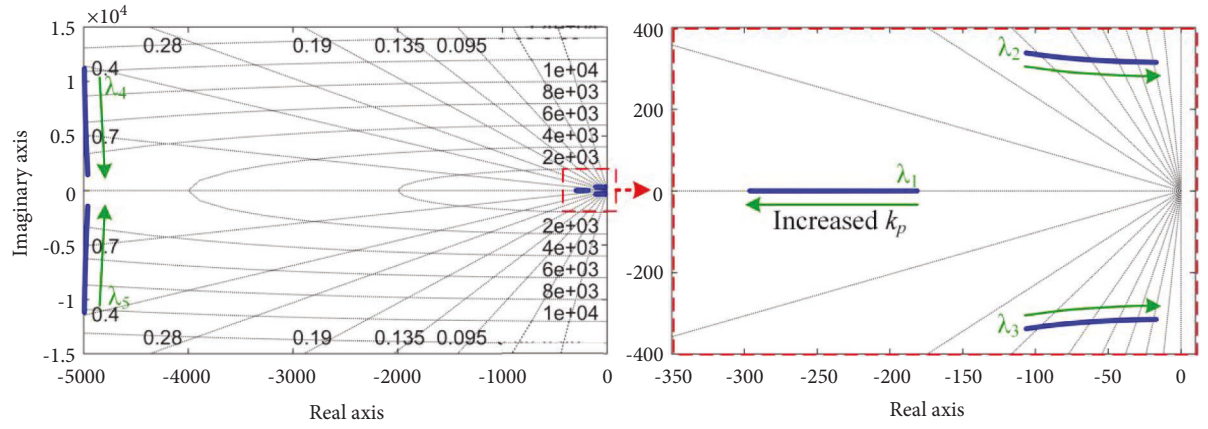

Figure 11: Generalized root locus diagram with a variation of k_p ($0.1 \le k_p \le 1.5$, $k_i = 100$, and $\omega_c = 5500$ rad/s).

According to (16) and (19), the control block diagram of the proposed method can be equivalently depicted in Figure 9. According to the superposition theorem, the closed-loop system can be represented as

$$v_o(s) = G_c(s)v_r(s) + Z(s)i_o(s)$$

$$= \frac{H(s)G_1(s)G_2(s)G_p(s)}{1 + G_2(s)G_p(s) + H(s)G_1(s)G_2(s)G_p(s)}v_r(s)$$

$$+ \frac{G_d(s)}{1 + G_2(s)G_p(s) + H(s)G_1(s)G_2(s)G_p(s)}i_o(s), \tag{20}$$

where $G_c(s)$ and $Z(s)$ denote the no-load voltage gain and the equivalent output impedance, respectively.

By replacing $i_o(s)$ with $v_o(s)/Z_l(s)$, where $Z_l(s)$ denotes the load, the transfer function $e(s)/v_r(s)$ can be obtained. Substituting $s = j\omega_f$ into it gives

$$\frac{e(s)}{v_r(s)}\Big|_{s=j\omega_f} = 0. \tag{21}$$

Therefore, the proposed control strategy can effectively eliminate the fundamental voltage tracking error, which means the advantage of SRFPI can be retained.

3.3. Stability and Dynamic Performance. Based on the stability criteria, the system in Figure 9 is stable if the closed-loop transfer function has no right half plane (RHP) poles.

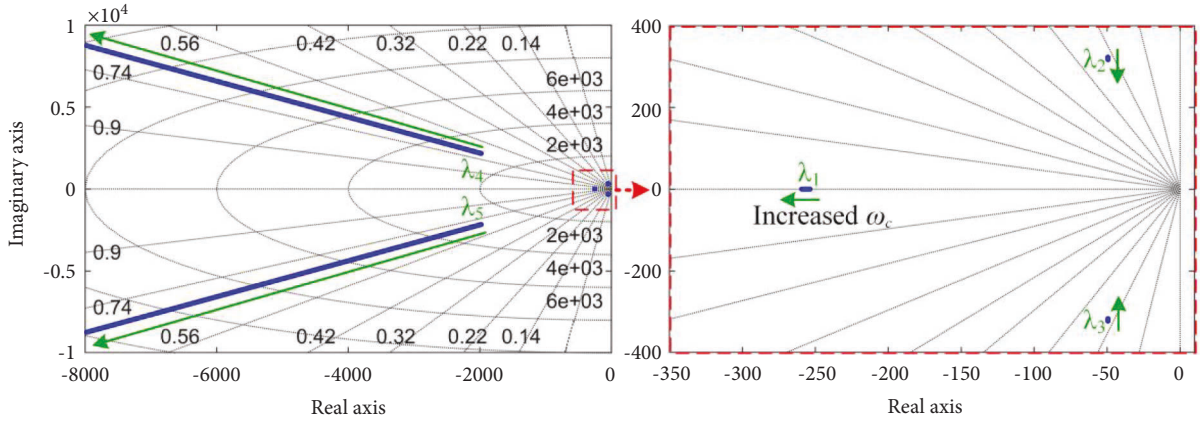

Figure 12: Generalized root locus diagram with a variation of ω_c ($2000 \leq \omega_c \leq 8000$ rad/s, $k_i = 100$, and $k_p = 1.5$).

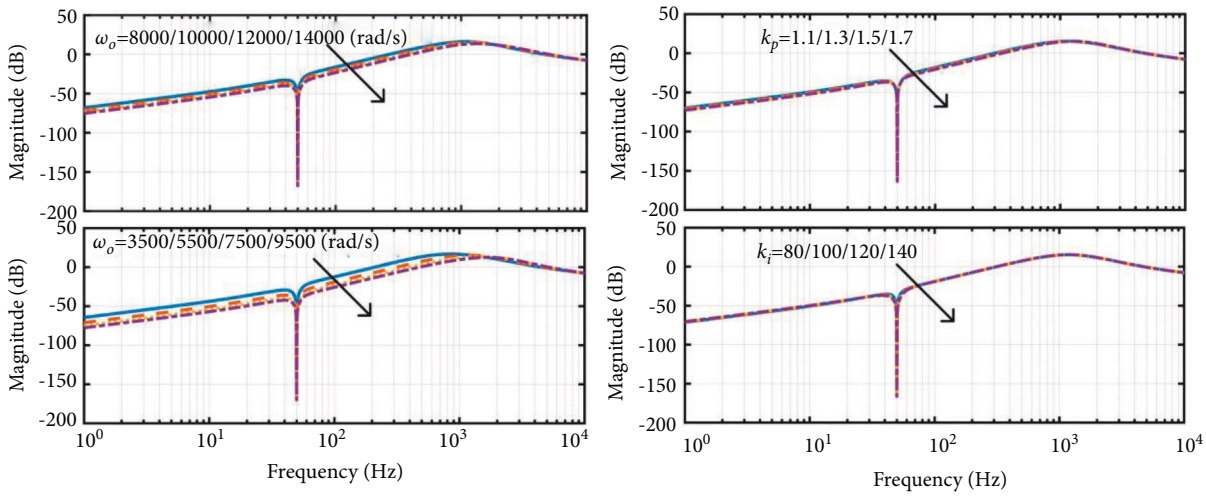

Figure 13: Bode magnitude plots of $v_o(s)/d(s)$. (a) Variation of ω_o and ω_c and (b) variation of k_p and k_i.

From (20), the characteristic polynomial of the closed-loop system can be derived as

$$s^5 + m_4 s^4 + m_3 s^3 + m_2 s^2 + m_1 s + m_0 = 0, \quad (22)$$

where $m_4 = k_2 + \omega_f$, $m_3 = \omega_f^2 + k_2\omega_f + k_1 + k_1k_p$, $m_2 = k_1k_i + k_1\omega_f + k_2\omega_f^2 + \omega^3{}_f + k_1k_p\omega_f$, $m_1 = 2k_1k_i\omega_f + k_1\omega^2{}_f + k_1k_p\omega^2{}_f + k_2\omega^3{}_f$, and $m_0 = k_1\omega^3{}_f - k_1k_i\omega^2{}_f + k_1k_p\omega^3{}_f$, respectively.

The stability and dynamic performance of the system with varied control parameters are given. The parameters of the inverter system are listed in Table 2. Figure 10 shows the root locus of the system under varied integral gain k_i, which changes from 10 to 500. The system remains stable since no poles exist in RHP. The dominant poles λ_1 and λ_2 move from right to left while λ_1 moves towards the imaginary axis indicating that the stability and dynamic performance of the system is improved with increased k_i within a certain range.

Figure 11 shows the root locus of the system under varied k_p, which changes from 0.1 to 1.5. The roots of characteristic polynomials all lie in the left half plane (LHP), which manifests the system and keeps stable. The system becomes more oscillatory since poles λ_2 and λ_3 are getting close to the imaginary axis, leading to the reduction of the damping ratio.

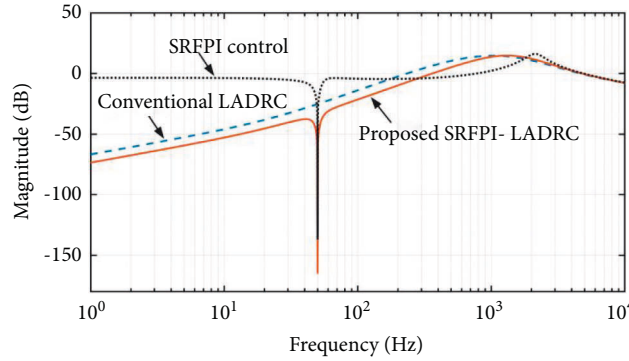

Figure 14: Bode magnitude plots of $v_o(s)/d(s)$ under different control strategies.

The root locus with ω_c increasing from 2000 to 8000 rad/s is shown in Figure 12. The system maintains stability. The damping ratio of the system is almost constant since the positions of the dominant poles λ_2 and λ_3 change little. The

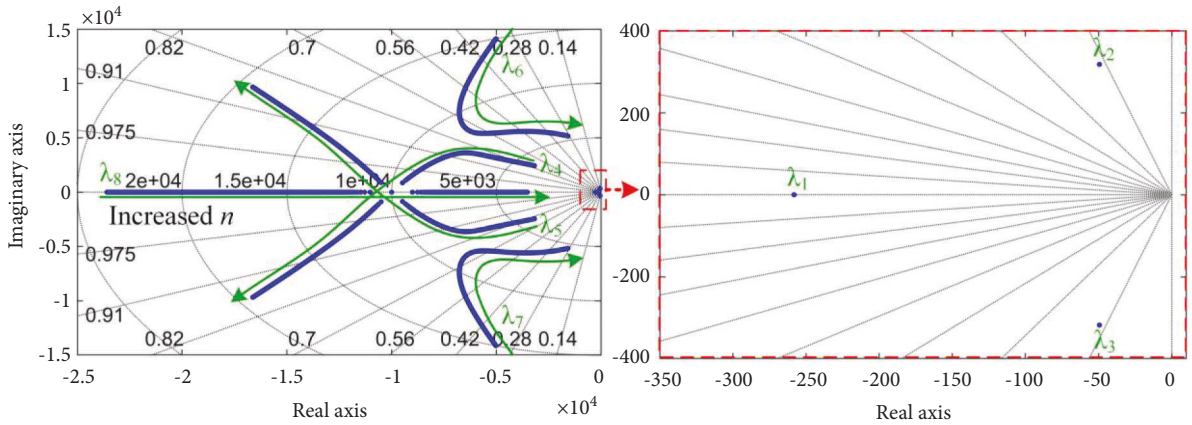

Figure 15: Generalized root locus diagram of $G_c(s)$ with a variation of n.

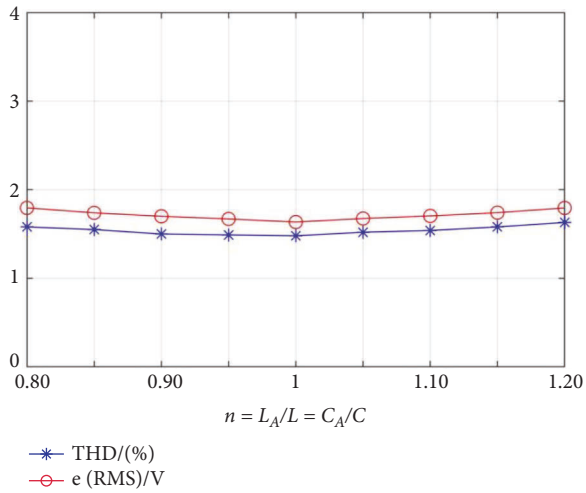

Figure 16: Perturbation of parameters under nominal resistive load conditions.

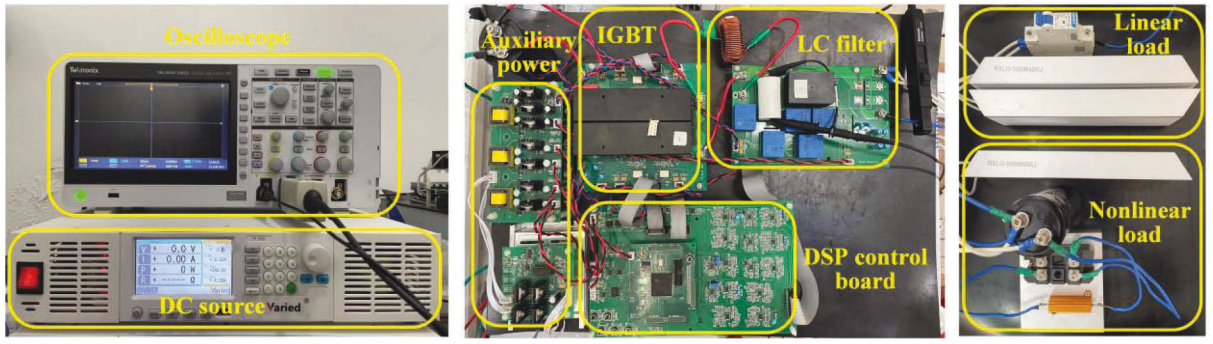

Figure 17: Experimental setup.

locus of pole λ_1 indicates that the settling time slightly gets shorter.

3.4. Disturbance Immunity Analysis. The disturbance rejection characteristics of the closed-loop system are investigated. The output current i_o is regarded as the external disturbance d. The transfer function $v_o(s)/d(s)$ can be obtained as

$$\frac{v_o(s)}{d(s)} = \frac{G_d(s)}{1 + G_2(s)G_p(s) + H(s)G_1(s)G_2(s)G_p(s)}. \quad (23)$$

tFigure 13 shows the amplitude-frequency diagram of $v_o(s)/d(s)$ with different controller parameters. As shown

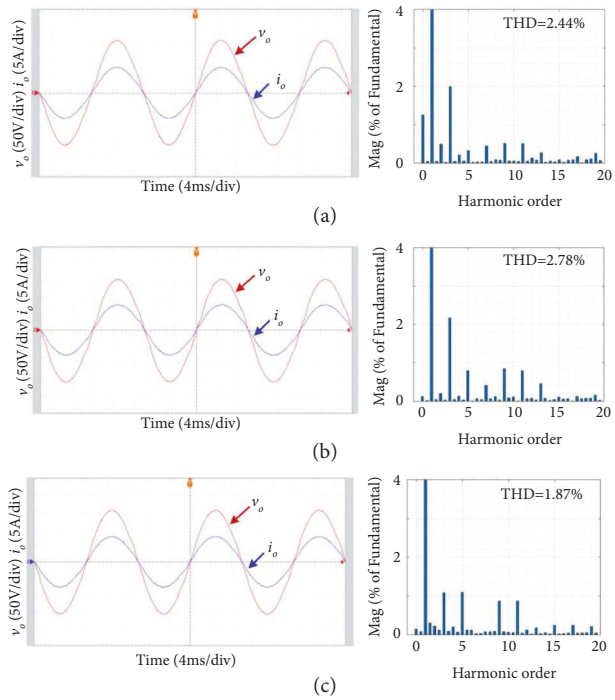

FIGURE 18: Steady-state waveforms of different control strategies under rated linear load (20 Ω). (a) SRFPI, (b) LADRC, and (c) proposed SRFPI-LADRC.

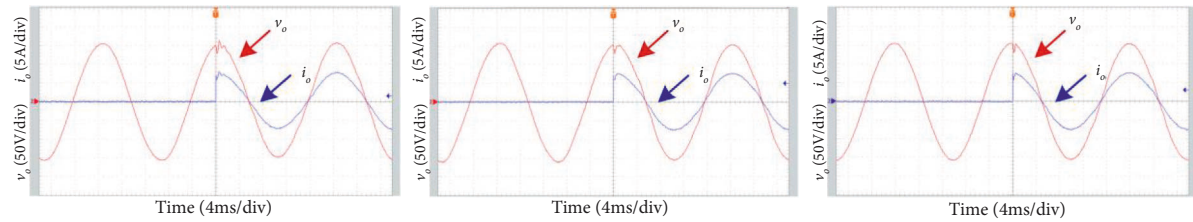

FIGURE 19: Transient waveforms in response to no load to rated load (20 Ω) step change. (a) SRFPI, (b) LADRC, and (c) proposed SRFPI-LADRC.

in Figure 13(a), with increase in the observer bandwidth ω_o and the controller bandwidth ω_c, the disturbance suppression ability of the system is enhanced. Furthermore, the parameters of k_p and k_i have little effect on the disturbance rejection as can be seen from Figure 13(b). Based on the above analysis, in this work, $\omega_c = 5500$ rad/s, $\omega_o = 10000$ rad/s, $k_i = 100$, and $k_p = 1.5$ are chosen, as listed in Table 2.

The comparison of disturbance-resistant performance under three control strategies is shown in Figure 14. The SRFPI control includes an inner capacitor current proportional loop [20], and the corresponding proportional gain is set as 3. Notice that the proposed SRFPI-LADRC has a better inhibition effect on disturbance at the low-frequency region, especially at the fundamental frequency.

3.5. Robustness Analysis. In practice, the parameters of the *LC* filter may vary because of aging and different operating conditions, which may deteriorate the system's performance. Considering the mismatch between the actual values (L_A, C_A) and nominal values (L, C), the robustness of the system is investigated. The parameter mismatch factor is defined as $n = L_A/L = C_A/C$. Considering that the parametric perturbation is usually within ±20%, [35] the generalized root locus under varied L_A and C_A, where n varies from -20% to +20%, is shown in Figure 15. The movement trajectory of the poles indicates that the system remains stable, which means the proposed controller is robust to parametric variations.

To verify the robustness of the proposed control strategy, a simulation model of a single-phase inverter system is built in MATLAB/Simulink environment, using the parameters listed in Table 2. The mismatch of *LC* parameters is considered under nominal resistive load (20 Ω). The results are shown in Figure 16, where the tracking error $e = v_o - v_r$, and e(RMS) denotes the root mean square (RMS) value of e. The system is robust against filter parameter perturbation.

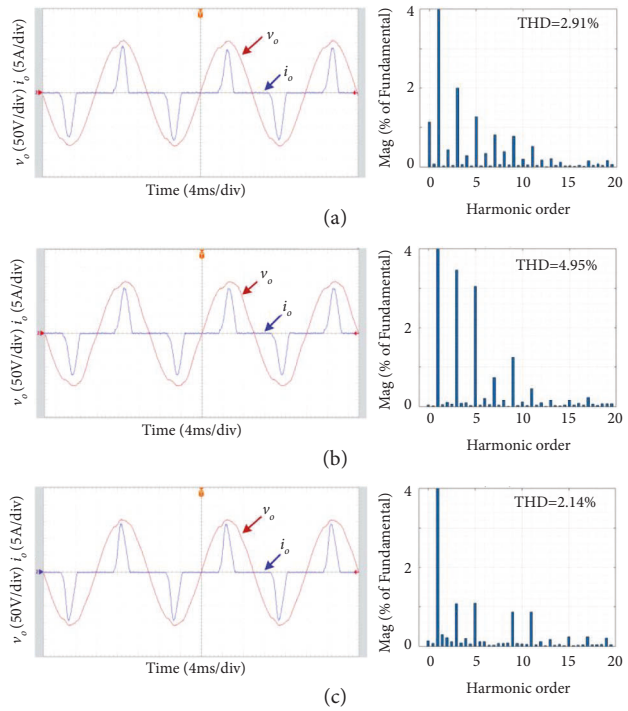

Figure 20: Steady-state waveforms of different control strategies under highly nonlinear load conditions. (a) SRFPI, (b) LADRC, and (c) proposed SRFPI-LADRC.

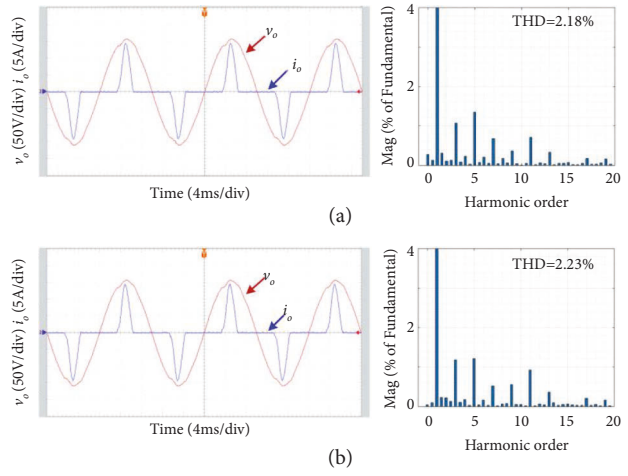

Figure 21: Steady-state waveforms with different L_A. (a) $L_A/L^{=}1.2$ and (b) $L_A/L = 0.8$.

Table 3: Performances of the three methods.

Load type	SRFPI			LADRC			SRFPI-LADRC		
	THD(%)	e_{rms}(V)	V_{orms}(V)	THD(%)	e_{rms}(V)	V_{orms}(V)	THD(%)	e_{rms}(V)	V_{orms}(V)
No load	1.60	1.65	110.52	2.20	13.40	111.74	0.87	1.38	110.52
Nominal resistive load	2.44	2.89	110.45	2.78	16.19	110.86	1.87	2.81	110.47
Highly nonlinear load	2.91	9.52	110.54	4.95	15.40	111.47	2.14	3.48	110.56
No load to rated load	Voltage restore time(ms)								
	1.6			1.2			0.8		

4. Experimental Results

According to the previous analysis, the output current caused by the loads or load variations can be seen as the main external disturbance, while the internal disturbances mainly refer to the dead time, parasitic parameters, parameter perturbation, and so on. These disturbances will deteriorate the system's performance.

To verify the effectiveness of the proposed control strategy, a 605-W single-phase inverter prototype was established as shown in Figure 17. The experimental setup is composed of a programmable dc power supply, a full-bridge IGBT module, an LC filter, an auxiliary power module, and a set of linear and nonlinear loads. The control algorithm is implemented in a DSP chip (TMS320F28335), and the digital oscilloscope is used to record the output voltage and current waveforms. The related parameters can be found in Table 2. The SRFPI control, the conventional LADRC, and the compound SRFPI-LADRC are tested and compared, and the SRFPI control includes an inner capacitor current proportional loop with a proportional gain of 3. To make the comparison persuasive, parameters of the overlapping parts of the three schemes stay consistent intentionally.

Figure 18 shows the experimental steady-state waveforms under a rated resistive load (20 Ω). Compared with the SRFPI and LADRC, the proposed method has the lowest THD (2.44% vs. 2.78% vs. 1.87%).

Figure 19 depicts the dynamic responses under a step load from no load to a rated load. The proposed method possesses the shortest transient response time (1.6 ms vs. 1.2 vs. 0.8 ms). In addition, it is noted that the voltage amplitude of the proposed method recovers in one period, which further illustrates its great performance against load disturbances.

Figure 20 shows the waveforms of output voltage and output current when feeding a highly nonlinear load, which consists of a 1-Ω resistor in series and a diode rectifier bridge feeding a 2700-μF capacitor in parallel with a 30-Ω resistor. All the output currents are significantly distorted with a crest factor approaching 3. Despite that, compared with SRFPI and LADRC, the output voltage of the proposed strategy represented a very small distortion (THD = 2.14%).

To verify the robustness of the proposed method, the waveforms under nonlinear load with L_A parameter variations (±20%) are shown in Figure 21. The steady-state waveforms indicate that the system remains stable and has small voltage THD (2.18% and 2.23%). In short, the SRFPI-LADRC has good robustness against system parameter perturbation.

The performances of the three methods, measured in terms of voltage THD, RMS values of output voltage, tracking error, and transient response time under a step load (from no load to a full load), are summarized in Table 3. It shows that the proposed SRFPI-LADRC scheme obtains overall performance improvement.

5. Conclusions

In this paper, a novel SRFPI-LADRC-based voltage control strategy is designed for an off-grid single-phase inverter. The main work and conclusions are summarized as follows:

(1) Inadequate ability to track a sinusoidal signal of traditional LADRC was analyzed. Then, an SRFPI controller is combined with LADRC to overcome its shortcomings. The proposed method includes only capacitor voltage loops. Thus, it does not require the generation of current quadrature signals and high-precision current sensors.

(2) The equivalent model of the inverter with the proposed compound control strategy is provided. The system stability, dynamic performance, and robustness are analyzed by means of the generalized root locus method, which show the superiority of the proposed scheme.

(3) Experimental results verified that the performances of the single-phase inverter with the proposed SRFPI-LADRC were markedly improved in comparison to conventional SRFPI and LADRC. The system achieved a very small steady-state error and voltage tracking error, as well as a fast dynamic response under load variations, and low THD (close to 2%) with highly nonlinear load.

(4) As a low-cost but high-performance solution, the proposed method is suitable for off-grid single-phase inverter applications, such as UPS inverters, outdoor portable power supplies, and vehicle inverters.

The performance verification of the proposed scheme for single-phase inverters mainly considers resistive loads and nonlinear loads. In future work, its performance under motor loads and during line-to-ground fault and the postfault recovery capability can be investigated. Furthermore, considering a single SRFPI controller only achieves satisfactory voltage control at the fundamental frequency; LADRC and multi-SRFPI-based compound control can be studied to achieve better harmonic compensation performance.

Abbreviations

v_o: Output voltage
i_o: Output current
f_1: Unknown system disturbance
f: Total system disturbance
u: Control signal
δ_u: Input disturbance
δ_y: Observation noise
ω_o: Observer bandwidth
ω_c: Controller bandwidth
x_1, $\hat{x}_1$, x_{e1}: Output voltage, observed voltage, and observation error
ω_f: Fundamental angular frequency; e, output voltage tracking error
r, v_r: Input reference voltage
L, C: Nominal filter inductance and capacitance values
L_A, C_A: Actual filter inductance and capacitance values
RMS: Root-mean-square
V_{orms}, e_{rms}: RMS values of output voltage and tracking error
ADRC: Active disturbance rejection control

LADRC: Linear ADRC
SRF: Synchronous reference frame
SRFPI: Synchronous reference frame proportional-integral
THD: Total harmonic distortion
PID: Proportional-integral-derivative
DBC: Deadbeat control
PR: Proportional-resonant
RC: Repetitive control
MPC: Model predictive control
LQG: Linear quadratic Gaussian
ESO: Extended sate observer
LESO: Linear extended state observer
MA-LESO: Model-assisted LESO
OSG: Orthogonal-signal-generation
APF: All-pass filter
UPS: Uninterrupted power supply.

Data Availability

All data generated or used during the study appear in the submitted article.

Conflicts of Interest

The authors declare that they have no conflicts of interest.

Acknowledgments

This work was supported by the National Natural Science Foundation of China under Grant no. 52007068 and the Fundamental Research Funds for the Central Universities under Grant no. ZQN-1007.

References

[1] K. Siraj, M. Awais, H. A. Khan et al., "Optimal power dispatch in solar-assisted uninterruptible power supply systems," *International Transactions on Electrical Energy Systems*, vol. 30, no. 1, 2020.

[2] M. Parvez, M. F. M. Elias, N. A. Rahim, F. Blaabjerg, D. Abbott, and S. F. Al-Sarawi, "Comparative study of discrete PI and PR controls for single-phase UPS inverter," *IEEE Access*, vol. 8, pp. 45584–45595, 2020.

[3] A. H. Eshghi, J. Soltani, M. M. Rezaei, and S. Shojaeian, "A robust control strategy for a single-phase grid-connected multibus microgrid based on adaptive sliding mode control and dynamic phasor concept," *International Transactions on Electrical Energy Systems*, vol. 31, no. 8, Article ID e12936, 2021.

[4] F. Nejabatkhah and Y. W. Li, "Flexible unbalanced compensation of three-phase distribution system using single-phase distributed generation inverters," *IEEE Transactions on Smart Grid*, vol. 10, no. 2, pp. 1845–1857, 2019.

[5] T. Bessaad, R. Taleb, F. Chabni, and A. Iqbal, "Fuzzy adaptive control of a multimachine system with single inverter supply," *International Transactions on Electrical Energy Systems*, vol. 29, no. 10, Article ID e12070, 2019.

[6] M. I. Azim, K. U. Z. Mollah, and H. R. Pota, "Design of a dynamic phasors-based droop controller for PV-based islanded microgrids," *International Transactions on Electrical Energy Systems*, vol. 28, no. 7, Article ID e2559, 2018.

[7] M. Izadi and A. Akbari Foroud, "Harmonic reduction of three-phase power inverter injection current using virtual admittance," *International Transactions on Electrical Energy Systems*, vol. 31, no. 2, Article ID e12739, 2020.

[8] Y. Allahvirdizadeh, H. Shayanfar, and M. Parsa Moghaddam, "A comparative study of PI, fuzzy-PI, and sliding mode control strategy for battery bank SOC control in a standalone hybrid renewable system," *International Transactions on Electrical Energy Systems*, vol. 30, no. 2, Article ID e12181, 2020.

[9] M. Trabelsi, L. Ben-Brahim, A. Gastli, and H. Abu-Rub, "Enhanced deadbeat control approach for grid-tied multilevel flying capacitors inverter," *IEEE Access*, vol. 10, pp. 16720–16728, 2022.

[10] S. J. Dai, J. B. Wang, Z. G. Sun, and E. Chong, "Deadbeat predictive current control for high-speed permanent magnet synchronous machine drives with low switching-to-fundamental frequency ratios," *IEEE Transactions on Industrial Electronics*, vol. 69, no. 5, pp. 4510–4521, 2022.

[11] R. Errouissi, H. Shareef, and A. Wahyudie, "A novel design of PR controller with anti-windup scheme for single-phase interconnected PV systems," *IEEE Transactions on Industry Applications*, vol. 57, no. 5, pp. 5461–5475, 2021.

[12] P. Alemi, C. J. Bae, and D. C. Lee, "Resonance suppression based on PR control for single-phase grid-connected inverters with filters," *IEEE Journal of Emerging and Selected Topics in Power Electronics*, vol. 4, no. 2, pp. 459–467, 2016.

[13] Y. Han, X. Fang, P. Yang, C. Wang, L. Xu, and J. M. Guerrero, "Stability analysis of digital-controlled single-phase inverter with synchronous reference frame voltage control," *IEEE Transactions on Power Electronics*, vol. 33, no. 7, pp. 6333–6350, 2018.

[14] W. Z. Lu, W. Wang, K. L. Zhou, and Q. Fan, "General high-order selective harmonic repetitive control for PWM converters," *IEEE Journal of Emerging and Selected Topics in Power Electronics*, vol. 10, no. 1, pp. 1178–1191, 2022.

[15] A. K. Pati and N. C. Sahoo, "A novel power quality enhancement scheme for three-phase differential boost inverter–based grid-connected photovoltaic system with repetitive and feedback linearizing control," *International Transactions on Electrical Energy Systems*, vol. 29, no. 5, Article ID e2832, 2019.

[16] B. Liu, D. He, G. Li, H. Liu, L. Yang, and Y. Chen, "Single-loop control for single-phase dual-boost grid-tied inverter with half cycle modulation and feedforward virtual-vectors MPC," *IEEE Transactions on Industrial Electronics*, vol. 69, no. 12, pp. 13918–13924, 2022.

[17] M. A. Rahman, M. A. Hossain, and M. M. Sikder, "A comparative study of robust optimal controllers for grid voltage control in islanded microgrids," in *Proceedings of the International Conference On Advancement In Electrical And Electronic Engineering (ICAEEE)*, Gazipur, Bangladesh, 2022.

[18] D. Zhi, "Optimization of PID controller for single phase inverter based on ABC," in *Proceedings of the 5th International Conference on Control, Automation and Robotics*, Beijing, China, 2019.

[19] D. N. Zmood and D. G. Holmes, "Stationary frame current regulation of PWM inverters with zero steady state error," *IEEE Transactions on Power Electronics*, vol. 18, no. 3, pp. 814–822, 2003.

[20] M. Monfared, S. Golestan, and J. M. Guerrero, "Analysis, design, and experimental verification of a synchronous

reference frame voltage control for single-phase inverters," *IEEE Transactions on Industrial Electronics*, vol. 61, no. 1, pp. 258–269, 2014.

[21] L. Callegaro, C. Rojas, M. Ciobotaru, and J. Fletcher, "A controller improving photovoltaic voltage regulation in the single-stage single-phase inverter," *IEEE Transactions on Power Electronics*, vol. 37, no. 1, pp. 354–363, 2022.

[22] J. Han, "From PID to active disturbance rejection control," *IEEE Transactions on Industrial Electronics*, vol. 56, no. 3, pp. 900–906, 2009.

[23] Z. Gao, "Scaling and bandwidth-parameterization based controller tuning," in *Proceedings of the 2003 American Control Conference*, Denver, CO, USA, 2003.

[24] Z. Gao, *Active Disturbance Rejection Control: A Paradigm Shift in Feedback Control System Design*, American Control Conference, Minneapolis, MN, USA, 2006.

[25] R. Zhou and W. Tan, "Analysis and tuning of general linear active disturbance rejection controllers," *IEEE Transactions on Industrial Electronics*, vol. 66, no. 7, pp. 5497–5507, 2019.

[26] R. Zhou, C. Fu, and W. Tan, "Implementation of linear controllers via active disturbance rejection control structure," *IEEE Transactions on Industrial Electronics*, vol. 68, no. 7, pp. 6217–6226, 2021.

[27] C. Liu, G. Luo, X. Duan, Z. Chen, Z. Zhang, and C. Qiu, "Adaptive LADRC-based disturbance rejection method for electromechanical servo system," *IEEE Transactions on Industry Applications*, vol. 56, no. 1, pp. 876–889, 2020.

[28] P. Lin, Z. Wu, Z. Fei, and X. M. Sun, "A generalized PID interpretation for high-order LADRC and cascade LADRC for servo systems," *IEEE Transactions on Industrial Electronics*, vol. 69, no. 5, pp. 5207–5214, 2022.

[29] J. Zeng, Z. L. Huang, Y. Y. Huang et al., "Modified linear active disturbance rejection control for microgrid inverters: design, analysis, and hardware implementation," *International Transactions on Electrical Energy Systems*, vol. 29, no. 9, Article ID e12060, 2019.

[30] Z. Xie, Y. Chen, W. Wu et al., "Admittance modeling and stability analysis of grid-connected inverter with LADRC-PLL," *IEEE Transactions on Industrial Electronics*, vol. 68, no. 12, pp. 12272–12284, 2021.

[31] R. Reaz, K. Reza, and B. Issa, "Linear active disturbance rejection control design for single-phase UPS inverters," in *Proceedings of the 47th Annual Conference of the IEEE Industrial Electronics Society*, Toronto ON Canada, 2021.

[32] Y. Cao, Q. Zhao, Y. Ye, and Y. Xiong, "ADRC-based current control for grid-tied inverters: design, analysis, and verification," *IEEE Transactions on Industrial Electronics*, vol. 67, no. 10, pp. 8428–8437, 2020.

[33] Q. Meng and Z. S. Hou, "Active disturbance rejection based repetitive learning control with applications in power inverters," *IEEE Transactions on Control Systems Technology*, vol. 29, no. 5, pp. 2038–2048, 2021.

[34] R. Y. Kim, S. Y. Choi, and I. Y. Suh, "Instantaneous control of average power for grid tie inverter using single phase D-Q rotating frame with all pass filter," in *Proceedings of the 30th Annual Conference of IEEE Industrial Electronics Society*, Busan, Korea, 2004.

[35] Y. Wu and Y. Ye, "Internal model-based disturbance observer with application to CVCF PWM inverter," *IEEE Transactions on Industrial Electronics*, vol. 65, no. 7, pp. 5743–5753, 2018.